Lagrangian versus Eulerian spectral estimates of surface kinetic energy over the global ocean

Xinwen Zhang[1], Xiaolong Yu[1], Aurélien L. Ponte[2], Zoé Caspar-Cohen[2,3], Sylvie Le Gentil[2], Lu Wang[2], Wenping Gong[1]

[1]School of Marine Sciences, Sun Yat-sen University, and Southern Marine Science and Engineering Guangdong Laboratory (Zhuhai), Zhuhai, China
[2]Ifremer, Université de Brest, CNRS, IRD, Laboratoire d'Océanographie Physique et Spatiale, IUEM, Brest, France
[3]Scripps Institution of Oceanography, University of California, San Diego, La Jolla, California, USA

Key Points:

- The accuracy of Lagrangian high-frequency kinetic energy estimates is evaluated with a novel twin global numerical simulation experiment.
- Lagrangian velocity spectra are smoother than Eulerian counterparts at tidal frequency peaks, but not at near-inertial ones.
- Lagrangian and Eulerian tidal energies agree better in regions characterized by weak low-frequency kinetic energy and high drifter density.

Corresponding author: Xiaolong Yu, yuxlong5@mail.sysu.edu.cn

Abstract

In this study, we carried out a novel massive Lagrangian simulation experiment derived from a global 1/48° tide-resolving numerical simulation of the ocean circulation. This first-time twin experiment enables a comparison between Eulerian (fixed-point) and Lagrangian (along-flow) estimates of kinetic energy (KE), and the quantification of systematic differences between both types of estimations. This comparison represents an important step forward for the mapping of upper ocean high-frequency variability from drifter database. Eulerian KE rotary frequency spectra and band-integrated energy levels (e.g., tidal and near-inertial) are considered as references, and compared to Lagrangian estimates. Our analysis reveals that, apart from the near-inertial band, Lagrangian spectra are systematically smoother, e.g., with wider and lower spectral peaks compared to Eulerian counterparts. Consequently, Lagrangian KE levels obtained from spectra band integrations tend to underestimate Eulerian levels on average at low-frequency and tidal bands. This underestimation is more significant in regions characterized by large low-frequency KE. In contrast, Lagrangian and Eulerian near-inertial spectra and energy levels are comparable. Further, better agreements between Lagrangian and Eulerian KE levels are generally found in regions of convergent surface circulation, where Lagrangian particles tend to accumulate. Our results demonstrate that Lagrangian estimates may provide a distorted view of high-frequency variance. To accurately map near-surface velocity climatology at high frequencies (e.g., tidal and near-inertial) from Lagrangian observations of the Global Drifter Program, conversion methods accounting for the Lagrangian bias need to be developed.

Plain Language Summary

Ocean surface currents play a pivotal role in transporting heat and energy across the global ocean, and thus affect global climate patterns and marine ecosystems. Yet, despite ocean currents' significant role in the Earth system, much of the rapid (high frequency) ocean variability is not known accurately at the moment. In this study, we show that the information derived from the movements of surface drifters, which track ocean currents, may help fill this gap. This is demonstrated with global ocean numerical models, which are now able to represent high-frequency variability associated with tides, winds and eddies, and are therefore powerful tools to evaluate ocean multi-scale variability. We compare here fixed-point (i.e., "Eulerian") and along-flow (i.e., "Lagrangian" or drifter) kinetic energy estimates. Our results show that the Lagrangian frame of reference can induce distortions of rapid motion signals when compared to Eulerian frame of reference, particularly in regions of large kinetic energy and low drifter density. Nevertheless, these two different perspectives can be reconciled in the estimation of energy levels, as long as adequate frequency bandwidths are chosen. This work highlights the potential of drifter-based observations in enhancing our understanding of high-frequency ocean variability.

1 Introduction

The ocean circulation controls the transport and distribution of physical properties and biochemical tracers across the global ocean. Ocean motions at horizontal scales smaller than several hundreds of kilometers and temporal scales shorter than months account for a dominant fraction of kinetic energy (KE; Ferrari & Wunsch, 2009). Its two main contributors are quasi-geostrophic balanced motions, which include mesoscale eddies (horizontal scales of 20-300 km, periods of weeks to months) and submesoscale motions (horizontal scales of 0.2-20 km, periods of hours to days), and unbalanced internal waves (horizontal scales <300 km and periods <1 day). Mesoscale eddies account for most of the global ocean KE and play a key role in the physical equilibrium and biogeochemical functioning of the ocean at climatic scales (McWilliams, 2008; McGillicuddy et al., 2007; Treguier et al., 2014). Submesoscale motions induce, on the other hand, a vigorous vertical circulation and determine the vertical exchanges of heat, carbon, and nutrients (McWilliams, 2016; Lévy et al., 2018; Taylor & Thompson, 2023). Internal waves are a major driver for turbulent mixing in the ocean, which is of fundamental importance to the global overturning circulation (Whalen et al., 2020). Internal waves are commonly organized around frequency, and are observed to have energy peaks at tidal and near-inertial frequencies, and a continuous energy distribution across higher frequencies, commonly known as the internal wave continuum.

Provided sufficient information is available along spatial and temporal dimensions, one way of characterizing quasi-geostrophic balanced motions and unbalanced internal waves is to estimate the distribution of surface KE as function of spatial and temporal scales. Torres et al. (2018) examined for instance the distribution of surface KE in wavenumber-frequency space from a high-resolution numerical simulation, and showed that lower-frequency motions emanate from larger scales and spread to finer spatial and temporal scales. The emergence of wide-swath altimetry and surface current measuring satellite missions has fostered efforts aiming at improving our understanding of oceanic variability down to O(10 km) and of its manifestation on satellite and in situ observations (Morrow et al., 2019; Du et al., 2021).

An emerging dataset to proceed with in situ observational descriptions across scales is that of the Global Drifter Program (GDP; Elipot et al., 2016). With the development of satellite tracking system, the GDP dataset provides global velocity measurements at hourly resolution, and thus enables studies of ocean variability at high frequencies. Yu et al. (2019) compared frequency spectra estimated from GDP drifter data (i.e., Lagrangian) and output from a high-resolution Massachusetts Institute of Technology general circulation model (MITgcm) simulation (i.e., Eulerian), which enable to point towards inaccurate representations of tidal and near-inertial variability in the numerical model. Arbic et al. (2022) performed a similar yet more detailed comparison based on Yu et al. (2019) datasets and an additional global tide-resolving simulation of the HYbrid Coordinate Ocean Model (HYCOM). In global maps and zonal averages, numerical models captured the low-frequency and high-frequency variance qualitatively. HYCOM simulation, because of its more frequently updated wind-forcing and a more finely tuned implementation of tidal variability, was found closer to GDP drifter values compared to MITgcm simulation. However, both studies questioned the equivalence between Eulerian and Lagrangian estimates, which has not been demonstrated yet.

Further, GDP drifter observations have been extensively used to achieve global and regional climatology of time-mean and mesoscale oceanic flows (Lumpkin & Johnson, 2013; Lumpkin, 2016), while such mapping at high frequencies remains relatively understudied (e.g., Liu et al., 2019). Understanding and quantifying the differences caused by Lagrangian inherent sampling nature with respect to Eulerian is a key step to ensure the rationality of the mapping of high-frequency variance using the GDP data. At semidiurnal frequencies, Caspar-Cohen et al. (2022) recently demonstrated that the displacement of surface drifters may distort low-mode internal tide signals which translated to wider spectral peaks, a mechanism coined “apparent incoherence”.

In this work, we compare Lagrangian and Eulerian spectral decompositions of surface KE at global scale, with the aid of output from a high-resolution ocean numerical model (LLC4320 simulation; Yu et al., 2019). A central question addressed here is whether high-frequency Eulerian KE levels can be accurately estimated from Lagrangian drifters. The paper is organized as follows. Section 2 describes the LLC4320 simulation, the Lagrangian numerical simulation experiments, and methods of spectral analysis and energy level estimates. Comparisons between Eulerian and Lagrangian KE fields are described in Section 3. Discussions and conclusions are given in Sections 4 and 5, respectively.

2 Materials and Methods

2.1 LLC4320 simulation

The LLC4320 simulation was performed using MITgcm (Marshall et al., 1997) on a global Latitude-Longitude-polar Cap (LLC) grid (Forget et al., 2015) for a period of 14 months between 10 September 2011 and 15 November 2012. The model has a horizontal grid spacing of 1/48° (approximately 2.3 km at the equator and 0.75 km in the Southern Ocean), and thereby resolves mesoscale eddies and permits submesoscale variability. The model time step was 25 seconds, and model variables were stored at hourly intervals. The model was forced by 6-hourly surface flux fields (including 10-m wind velocity, 2-m air temperature and humidity, downwelling long- and short-wave radiation, and atmospheric pressure load) from the European Centre for Medium-Range Weather Forecasts (ECMWF) operational reanalysis, and included the full lunisolar tidal constituents that are applied as additional external forcing. The LLC4320 uses a flux-limited monotonicity-preserving (seventh order) advection scheme, and the modified Leith scheme of Fox-Kemper and Menemenlis (2008) for horizontal viscosity. The K-profile parameterization (Large et al., 1994) is used for vertical viscosity and diffusivity. In this study, we use a yearlong record of the instantaneous surface fields at every hour, starting on 15 November 2011.

2.2 Lagrangian experiments

Lagrangian simulations are performed with LLC4320 hourly surface velocity outputs using the 'Parcels' Python package (Lange & Van Sebille, 2017; Delandmeter & Van Sebille, 2019). Surface virtual drifters are initially released every 50 grid points of LLC4320 grid (about 50 to 100 km spacing), and drifter positions and velocity fields are stored at hourly rate. The Lagrangian simulation is about one year long (from 15 November 2011 to 9 November 2012). Virtual drifters are released every 10 days at initial release positions if no virtual drifter is present within a radius equal to the distance to closest neighbor at initial release. This continuous seeding enables to maintain a continuous coverage throughout the Lagrangian simulation. The number of virtual drifters is of about 60,000 at the start, and reaches about 95,000 drifters at the end of the simulation. The Lagrangian particles in the LLC4320 simulation (i.e., virtual drifters) are scattered throughout the open ocean worldwide (Figure 1; also see Movie S1 in Supporting Information), and their spatial distribution is broadly in line with that of GDP drifters over the global ocean albeit with an instantaneous drifter density larger by about two orders of magnitudes (Elipot et al., 2016; Yu et al., 2019). Heavily sampled regions concentrate in flow convergence zones (e.g., the interior of subtropical gyres). In contrast, areas of flow divergence (e.g., the equatorial region, upwelling areas) as well as polar and coastal regions are generally less sampled. As a result, the number of 60-day particle trajectory segments at midlatitudes (30°-60°N and S) is at least a factor of 2 larger than that in the equatorial region (10°S-10°N).

2.3 Frequency rotary spectrum and bandwidth selection for energy integration

For Eulerian estimates, hourly surface horizontal velocity time series are used to compute rotary spectra of horizontal velocity at each model grid point. For Lagrangian esti-

mates, rotary spectra are computed from horizontal velocities along particle trajectories. For both datasets, we first divide velocity time series into segments of 60 days overlapping by 50% and linearly detrend over each segment, and then compute the 1D discrete Fourier transform of complex-valued fields ($u+iv$, where u and v are zonal and meridional velocity, respectively) multiplied by a Hanning window. Spectra are formed by multiplying Fourier amplitudes by their complex conjugates and averaged over time for Eulerian estimates and according to segment mean drifter's latitudes and longitudes for Lagrangian estimates (Figure 1b). Given the geographical distribution of particle trajectories, velocity data in polar regions with latitude higher than 60° and in coastal waters with depth shallower than 500 m are not considered in the calculation for both datasets.

Rotary frequency spectral densities are integrated over four frequency bands to compute KE components of interest, including high-frequency (>0.5 cpd, absolute values here and hereinafter), semidiurnal, near-inertial, diurnal bands. Total KE is estimated from temporal averages of instantaneous velocity fields, and low-frequency KE is computed as total KE minus high-frequency KE. We examine the sensitivity of the regression coefficient and root mean square error between Eulerian and Lagrangian semidiurnal, near-inertial and diurnal KE levels to different frequency bandwidths of integration (Figure 2). For semidiurnal band, the closest match between Eulerian and Lagrangian energy levels is achieved for the ±0.3 cpd bandwidth with a regression coefficient value closest to unity and a root mean square error plateauing at approximately 10^{-3} m^2 s^{-2} (equivalent to 15.6% of the averaged Eulerian semidiurnal energy level). In contrast, for diurnal and near-inertial bands, the narrowest bandwidth (i.e., ±0.1 cpd) yields the best comparison based on the two metrics. Consequently, the semidiurnal, near-inertial, diurnal bands are respectively defined as 1.7-2.3 cpd, 0.9-1.1f and 0.9-1.1 cpd, where f is the Coriolis frequency.

To achieve a balance between drifter density and spatial variability of bin-averaged diagnostics, a bin size of 1° latitude is employed to compare Eulerian and Lagrangian zonally averaged rotary spectra and associated band integrals. For global maps, the band-integrated KE estimates are averaged in 1°× 1° spatial bins. Finally, following Arbic et al. (2022), we compute the ratio of Lagrangian KE divided by the sum of Lagrangian and Eulerian KE. Note that a ratio of 0.5 indicates equality between Lagrangian KE and Eulerian KE, a ratio exceeding 0.5 indicates Lagrangian KE overestimates Eulerian KE, and a ratio below 0.5 indicates Lagrangian KE underestimates Eulerian KE.

3 Results

3.1 Zonally-averaged spectrum and KE

Lagrangian and Eulerian zonally averaged spectra both show expected peaks at low, near-inertial and tidal frequencies (Figures 3a and 3b). Along with Figures 3c and 3d, Lagrangian spectral peaks appear to be systematically broader and weaker than Eulerian ones, indicating a spreading of energy in the Lagrangian perspective. This spreading is clear around main tidal peaks and increases with frequency such that Lagrangian higher frequency tidal constituents (e.g. 3 cpd, 4 cpd, ...) are hardly noticeable unlike Eulerian ones. The ratio of Lagrangian to Eulerian spectra consistently indicates that Lagrangian peak values at tidal frequencies are lower but wider than Eulerian ones (Figure 3c). This is in line with the findings of Zaron and Elipot (2021), which noted that the drifter tidal peaks do not stand out above the background spectrum as strongly as in tide model predictions. Caspar-Cohen et al. (2022) consistently demonstrated that the distortion of tidal internal waves induced by surface drifter motions, a process coined as apparent incoherence, leads to broader tidal peaks.

At subinertial frequencies, a similar mechanism may be invoked to explain the smoothing of the low-frequency energy peak in Lagrangian diagnostics: Lagrangian particles sample both spatial and temporal variability, which leads to shorter velocity decorrelation timescales

and broader spectra (Middleton, 1985; Davis, 1983; Lumpkin et al., 2002; LaCasce, 2008). At near-inertial frequencies, the smoothing of the peak is not visible in latitude dependent spectra (Figures 3a and 3b), and the ratio of Lagrangian to Eulerian spectra indicates values close to unity (Figure 3c). This suggests that drifter displacements do not distort the signature of near-inertial waves similarly to internal tides, in line with findings from Shakespeare et al. (2021). Another obvious contrast is that energy levels at the anticyclonic frequencies are substantially higher than those at the cyclonic frequencies, particularly below the semidiurnal frequency band (Figure 3d). This conforms expectations from the natural polarization of internal gravity waves which leads to a ratio between anticyclonic and cyclonic kinetic energies that scales as $(\omega + f)^2/(\omega - f)^2$ (Gill, 1982; van Haren, 2003), where ω is the frequency, and is consistent with the observational findings of elevated near-inertial KE in the anticyclonic domain (Elipot et al., 2010; Vic et al., 2021; Yu et al., 2022).

Zonally averaged low-frequency, semidiurnal, near-inertial, diurnal KE estimated from Eulerian velocity field and Lagrangian particle trajectories with ("2D binned") and without ("raw") spatial binning are displayed in Figure 4. The overall trends of the Eulerian and Lagrangian (with and without binning) estimates show good visual similarities. Raw Lagrangian estimates tend to underestimate KE compared to 2D binned Lagrangian estimates, particularly at low-frequency energy peaks. Low-frequency energy peaks near the equator, at 35°N and 55°S at the locations of Northern Hemisphere western boundary currents and the Antarctic Circumpolar Current respectively (Figure 4a). At 35°N, Lagrangian energies underestimate Eulerian ones, which will be argued to partly result from the unequal sampling of high vs low energy regions (Davis, 1985) and may be mitigated with alternative geographical binning (see Discussion section). Lagrangian zonally averaged semidiurnal KE is slightly lower than Eulerian KE at almost all low and mid-latitudes (Figure 4b). In contrast, Lagrangian zonally averaged near-inertial KE follow Eulerian estimates relatively well over most latitudes, except for a clear underestimation near 30°S, where the local inertial frequency coincides with diurnal frequencies (Figure 4c). For the diurnal KE, discrepancies are relatively larger, with a 15.4% difference in average (Figure 4d), compared to low-frequency (7%), semidiurnal (11.1%), and near-inertial (6.7%) bands. There are two substantial mismatches between Eulerian and Lagrangian diurnal KE, one is in 20°N, which may be associated with the less Lagrangian particles in Luzon strait, and one is in 30°S, in line with the underestimation in near-inertial KE.

3.2 Low-frequency KE maps

Global maps of low-frequency KE highlight prominent large-scale currents and energetic areas, including equatorial and western boundary currents such as the Gulf Stream and the Antarctic Circumpolar Current (Figures 5a and 5b). Low-frequency KE dominates total energy and therefore mimic total KE variations (cf. Figures 1a and 5a). Lagrangian and Eulerian low-frequency KE are generally in good agreement, with a mean value and standard deviation of the ratio of Lagrangian KE/(Lagrangian KE+Eulerian KE) about 0.49 and 0.07, respectively (Figures 5c and 5d). A noticeable difference is that Lagrangian estimates appear smoother than Eulerian ones around large-scale current features, which presumably results from the spatial advection of Lagrangian particle over the temporal window of energy integration.

We next examine the dependence of the ratio of Lagrangian KE/(Lagrangian KE+Eulerian KE) on two factors, the number of Lagrangian particles per bin (i.e., drifter density) and the intensity of low-frequency KE. As the number of Lagrangian particles increases, the mean ratio gradually approaches 0.5, and the ratio range is more concentrated (Figure 5e). This suggests that Lagrangian KE tends to align more closely with Eulerian KE in regions where Lagrangian particles accumulate, indicating convergence of the flow. Further, the ratio exhibits a more pronounced dependence on the intensity of low-frequency KE. In regions of strong low-frequency flow, the ratio is significantly reduced, with a mean value smaller than 0.4, indicating a substantial underestimation of low-frequency KE from a Lagrangian

perspective (Figure 5f). This underestimation results from a larger projection of spatial variability onto temporal one along particle trajectories in energetic regions (LaCasce, 2008; Caspar-Cohen et al., 2022). Indeed, nearby energetic current features, Lagrangian energy thus tends to underestimate Eulerian energy maxima in the core of these features (ratio below 0.5) and overestimate Eulerian energy on the surroundings (ratio above 0.5; Figure 5c).

3.3 Semidiurnal KE maps

Semidiurnal, diurnal and near-inertial KE are all an order of magnitude smaller than low-frequency KE. The comparison between Lagrangian and Eulerian semidiurnal KE estimates show significant similarities globally (Figures 6a and 6b). Both clearly display hotspots of internal tide generation, e.g., near Hawaii islands, the French Polynesian islands, the Aleutians island chain, 40°S and 40°N in the Atlantic as well as the western Pacific. The discrepancies at semidiurnal frequencies are relatively larger compared to low frequencies, with a mean energy ratio of 0.47 and standard deviation of 0.06. Figures 6c and 6d show that Lagrangian semidiurnal KE systematically underestimate Eulerian semidiurnal KE, particularly in the ocean's major current regions of high kinetic energy. Noticeable differences between Lagrangian and Eulerian estimates also occur near coastal areas, where the Lagrangian field may exhibit semidiurnal KE levels considerably larger than the Eulerian field. This overestimate is likely to result from Lagrangian particles crossing continental shelves, where tidal currents are faster, over the 60-day window of energy integration.

Interestingly, for semidiurnal tides, the dependence of the ratio on the drifter density is relatively weak, although there is a slight increase in the ratio towards 0.5 with increasing particle counts (Figure 6e). Instead, the ratio shows a clear decreasing and scattering trend as the low-frequency KE intensity increases (Figure 6f). That is, the ratio ranges from about 0.23 to 0.67 with a mean value somewhat smaller than 0.5 in areas of strong low-frequency KE, while the range of the ratio reduces to 0.34 and 0.61 with a mean value closer to 0.5 in areas of weak low-frequency KE. This indicates that the bandwidth tuned based on a global criterion is likely not sufficient in areas of strong low-frequency KE to account for the smearing of the semidiurnal tidal spectral peak (Figure 3d).

3.4 Diurnal KE maps

The global map of diurnal Lagrangian KE also closely reproduces the Eulerian KE visually (Figures 7a and 7b). The most prominent feature of diurnal KE is the enhancement around $\pm 30^\circ$ latitudes, where the diurnal wind-forcing (sea breeze) aligns with the local inertial frequency. Similar to the semidiurnal band, the Lagrangian field shows larger values than the Eulerian field in several coastal regions (Figure 7c). These coastal regions are mostly located outside 30°S and 30°N, where diurnal internal tides are not expected to freely propagate, indicating that their differences may be caused by barotropic tides or trapped baroclinic tides. Over the global ocean, Lagrangian diurnal KE slightly underestimate Eulerian one (Figure 7d).

Similar to low-frequency motions, diurnal tides show a clear dependence on the drifter density and the intensity low-frequency KE (Figures 7e and 7f). For diurnal tides, the ratio of Lagrangian KE/(Lagrangian KE+Eulerian KE) gradually inclines towards 0.5 with the increase in Lagrangian particle counts, and becomes more focused on 0.5 with the decrease in low-frequency KE. In other words, Lagrangian diurnal KE matches Eulerian KE better in regions of weak and convergent flows, and tends to underestimate in regions of strong and divergent flows. This may explain the underestimation of Lagrangian diurnal KE in the Luzon Strait (approximately 20°N; Figure 4d), where the background flow is strong and divergent. Lastly, apparent incoherence is in general expected to be weaker at diurnal frequencies than at semidiurnal frequencies, due to the larger horizontal wavelength of diurnal tides (Caspar-Cohen et al., 2022).

3.5 Near-inertial KE maps

Lagrangian and Eulerian estimates of near-inertial KE show particularly similar spatial patterns across the global ocean (Figures 8a and 8b). Intensified near-inertial KE generally occurs at mid latitudes, with largest values concentrated in the North Pacific. This is broadly in line with storm-track regions and spatial distribution of wind work (Alford, 2003). Expected enhancements also occur at $\pm 30^{\circ}$ latitudes where the local inertial frequency coincides with diurnal frequencies. Nearly meridionally oriented beams appear in the low to mid latitudes and are particularly evident in the Eulerian field, likely associated with individual tropical cyclones and storms in the model forcing fields. The mean value and standard deviation of the energy ratio are 0.49 and 0.07, respectively (Figure 8c). Differences between Eulerian and Lagrangian near-inertial KE are modest in global maps compared to those within semidiurnal and diurnal bands. And this also embodies in Figure 8d, in which Eulerian and Lagrangian near-inertial KE closely follow a 1-to-1 relationship. Nonetheless, Lagrangian energy slightly underestimates near-inertial KE over open ocean regions in the Southern Hemisphere, around 30°S. It is probably related to the influence of diurnal bands and a change in the nature of motions (larger contribution from internal tides for instance).

Similar to low-frequency and tidal motions, the ratio of Lagrangian KE/(Lagrangian KE+Eulerian KE) in the near-inertial band also shows a dependence on the drifter density (Figure 8e). The mean ratio approaches 0.5 and the entire range becomes more focused on 0.5 with the increasing number of Lagrangian particles. However, there is no apparent association between the ratio and the intensity of low-frequency KE (Figure 8f).

4 Discussion

In previous studies, ocean surface KE in high-resolution global simulations has been compared with KE from GDP surface drifters (Yu et al., 2019; Arbic et al., 2022). Model-drifter comparisons showed good qualitative agreement over a wide range of frequency bands but systematic discrepancies were also observed, and the pending question is whether these discrepancies could be attributed to Lagrangian/Eulerian biases. We find that the difference between Lagrangian and Eulerian KE levels in LLC4320 is significantly lower than the one observed in model-drifter analysis. As in the comparison between LLC4320 and GDP drifters, a deficit of low-frequency energy within the equatorial region was observed, with energy peak values reaching 0.15 $m^2\ s^{-2}$ for the model and 0.34 $m^2\ s^{-2}$ for GDP drifters (Yu et al., 2019). This difference (approximately 0.2 $m^2\ s^{-2}$) is one order of magnitude larger than the Lagrangian-Eulerian difference near the equator, which is of order 0.01 $m^2\ s^{-2}$ as shown in Figure 4a. Moreover, Yu et al. (2019) reported that the LLC4320 simulation exhibits KE four times higher in the semidiurnal band and three times lower in the near-inertial band compared with GDP drifter data. However, the global mean ratios of Lagrangian KE to Lagrangian KE+Eulerian KE obtained in this study are 0.47 ± 0.06 for the semidiurnal band (Figure 6c) and 0.49 ± 0.07 for the near-inertial band (Figure 8c), both of which are close to 0.5. This means that, on average, Lagrangian KE is nearly equal to Eulerian KE for the semidiurnal and near-inertial bands in the LLC4320 simulation. Therefore, our results suggest that Lagrangian/Eulerian biases are very likely not the main cause of the model-drifter discrepancies.

Arbic et al. (2022) identified the sensitivity of the Lagrangian semidiurnal energy estimate to the bandwidth of integration, which the present study corroborates. This sensitivity arises from apparent incoherence which leads to a widening of the semidiurnal tidal peak (Caspar-Cohen et al., 2022). A single common value (i.e., 1.7-2.3 cpd) for the bandwidth of integration that produced the best match between Lagrangian and Eulerian energy estimates was chosen in the present study. However, the bandwidth of integration may not be the same for Eulerian and Lagrangian energy diagnostics. Limiting bandwidth may be desirable in order to mitigate contamination from the background energy spectrum. Given the sharper shape of Eulerian semidiurnal peaks, smaller bandwidths may be afforded for

Eulerian diagnostics. The width of Eulerian semidiurnal peaks is related to internal tide incoherent timescales, whose geographical variations may lead to geographically varying choices for the bandwidth of integration of Eulerian energy. Caspar-Cohen et al. (2022) theoretically predict that the intensity of apparent incoherence and thus the associated widening of the Lagrangian spectrum depends on parameters that may vary geographically such as the low-frequency energy level and decorrelation timescale or internal tide properties (wavenumber, incoherent timescale). The bandwidth of integration of Lagrangian estimates may thus be modulated geographically in order again to mitigate contamination from the background energy spectrum. Such more advanced choices for bandwidth of energy integration would be good material for future studies, even though the present study indicates this would be mostly relevant for the semidiurnal band which exhibits most sensitivity to integration bandwidth.

Lastly, Lagrangian low-frequency KE estimates considerably underestimate Eulerian ones in energetic regions (Figure 4a and 5f), likely due to the preferential sampling of weak-energy regions by Lagrangian particles (Freeland et al., 1975). The deficit caused by the inhomogeneous sampling of Lagrangian particles, in KE levels of up to 20%, can be compensated by averaging Lagrangian diagnostics into longitude/latitudes bins. Our recommendation is to geographically bin energy estimates prior to integration over larger domains (e.g., zonally, globally) to mitigate such sampling biases. However, it should be noted that along a similar line but at the bin level, the combination of spatio-temporal inhomogeneities and energy variability within individual bins may also lead to systematic differences between Eulerian and Lagrangian estimates (Davis, 1991), such as those observed nearby large current systems. The role of such sampling bias in explaining observed differences has not been investigated here but could constitute an interesting follow up study. Further, we have chosen here a 60-day time window for spectral decompositions and energy estimates, and this choices induces spatial smoothing compared to Eulerian estimates. Above-mentioned study may be useful in order to identify whether statistical techniques enabling more local (temporally and therefore spatially for drifters) estimates of high-frequency energy levels should be devised.

5 Summary

In this study, we quantify the relationship between Eulerian and Lagrangian KE spectral content and its geographical variability based on a novel twin global numerical simulation experiment. A practical objective is to assess the extent to which Lagrangian particles can estimate Eulerian KE levels, especially at high frequencies. To achieve this, we have compared the surface KE estimated using the LLC4320 global ocean model, and the Lagrangian simulations performed by the LLC4320 hourly surface velocity output. Our main findings are summarized as follows:

1) Eulerian and Lagrangian KE exhibit broad qualitative similarities, with the dominance of low-frequency motions and the presence of distinct spectral peaks at semidiurnal, near-inertial, and diurnal frequencies. A common feature among all dominant frequency bands is that Lagrangian spectra appear smoothed compared to Eulerian ones. This smoothing is least pronounced in the near-inertial band and most pronounced in the semidiurnal and low-frequency bands. At low frequencies, this smoothing is attributed to the simultaneous sampling of spatial and temporal variability by particles and the associated decrease in the decorrelation timescale (Middleton, 1985; LaCasce, 2008). The widening of the semidiurnal peak is consistent with the mechanism of apparent incoherence (Caspar-Cohen et al., 2022). The relatively minor difference between the Lagrangian and Eulerian near-inertial frequency peaks remains to be explained.

2) With a tuned choice of bandwidth of integration, good agreements for semidiurnal (1.7-2.3 cpd), near-inertial (0.9-1.1f) and diurnal (0.9-1.1 cpd) KE can be achieved between Eulerian and Lagrangian simulations. This implies that Lagrangian particles advected by

Eulerian filed can qualitatively reproduce the original Eulerian high-frequency variance. Compared to Eulerian estimates, Lagrangian estimates are more sensitive to bandwidth, as expected from their character of broadened spectral peaks. Particularly, Lagrangian semidiurnal tides are featured with a wider bandwidth than other high-frequency motions. We have identified avenues to refine further this choice of bandwidth of integration.

3) The intensity of low-frequency motions affects Lagrangian KE estimates at low and tidal frequencies. Lowest Lagrangian to Eulerian energy ratio is observed in energetic and turbulent areas. Conversely, Lagrangian KE in near-inertial band has no clear connection with low-frequency KE. For all bands, Lagrangian and Eulerian KE levels have a better agreement in regions of convergent flows, where Lagrangian particles accumulate, than in regions of divergent flows, where Lagrangian particles scatter.

Our findings confirm that the drifter data may provide an estimate of high-frequency variance, such as tidal and near-inertial motions. Drifter and model differences, as shown in Yu et al. (2019) and Arbic et al. (2022), are not mainly caused by Lagrangian vs Eulerian sampling nature. This work may motivate future studies on particular aspects of the model-observation and model-model discrepancies, and is a substantial step towards the production of high frequency KE climatologies.

Acknowledgments

This work was funded by grants from the National Natural Science Foundation of China (42206002, 42361144844), and Guangdong Basic and Applied Basic Research Foundation (2023A1515010654). This work was also supported by ANR project 17-CE01-0006-01 entitled EQUINOx (Disentangling Quasi-geostrophic Motions and Internal Waves in High Resolution Satellite Observations of the Ocean).

Open Research

The LLC4320 simulation output is available at https://data.nas.nasa.gov/ecco/data.php.

References

Alford, M. H. (2003). Redistribution of energy available for ocean mixing by long-range propagation of internal waves. *Nature*, *423*(6936), 159-162.

Arbic, B. K., Elipot, S., Brasch, J. M., Menemenlis, D., Ponte, A. L., Shriver, J. F., ... Nelson, A. D. (2022). Near-surface oceanic kinetic energy distributions from drifter observations and numerical models. *Journal of Geophysical Research: Oceans*, *127*(10), e2022JC018551.

Caspar-Cohen, Z., Ponte, A., Lahaye, N., Carton, X., Yu, X., & Gentil, S. L. (2022). Characterization of internal tide incoherence: Eulerian versus Lagrangian perspectives. *Journal of Physical Oceanography*, *52*(6), 1245-1259.

Davis, R. E. (1983). Oceanic property transport, Lagrangian particle statistics, and their prediction. *Journal of Marine Research*, *41*, 163-194.

Davis, R. E. (1985). Drifter observations of coastal surface currents during CODE: The statistical and dynamical views. *Journal of Geophysical Research: Oceans*, *90(C3)*, 4756-4772.

Davis, R. E. (1991). Observing the general circulation with floats. *Deep Sea Research Part A. Oceanographic Research Papers*, *38*, S531-S571.

Delandmeter, P., & Van Sebille, E. (2019). The Parcels v2.0 Lagrangian framework: new field interpolation schemes. *Geoscientific Model Development*, *12*(8), 3571-3584.

Du, Y., Dong, X., Jiang, X., Zhang, Y., Zhu, D., Sun, Q., ... Peng, S. (2021). Ocean surface current multiscale observation mission (OSCOM): Simultaneous measurement of ocean surface current, vector wind, and temperature. *Progress in Oceanography*, *193*, 102531.

Elipot, S., Lumpkin, R., Perez, R. C., Lilly, J. M., Early, J. J., & Sykulski, A. M. (2016). A global surface drifter data set at hourly resolution. *Journal of Geophysical Research: Oceans*, *121*(5), 2937-2966.

Elipot, S., Lumpkin, R., & Prieto, G. (2010). Modification of inertial oscillations by the mesoscale eddy field. *Journal of Geophysical Research: Oceans*, *115*(C9).

Ferrari, R., & Wunsch, C. (2009). Ocean circulation kinetic energy: Reservoirs, sources, and sinks. *Annual Review of Fluid Mechanics*, *41*, 253-282.

Forget, G., Campin, J. M., Heimbach, P., Hill, C. N., Ponte, R. M., & Wunsch, C. (2015). ECCO version 4: an integrated framework for non-linear inverse modeling and global ocean state estimation. *Geoscientific Model Development*, *8*(10), 3071-3104.

Fox-Kemper, B., & Menemenlis, D. (2008). Can large eddy simulation techniques improve mesoscale rich ocean models? In *Ocean modeling in an eddying regime* (p. 319-337). American Geophysical Union (AGU).

Freeland, H. J., Rhines, P. B., & Rossby, T. (1975). Statistical observations of the trajectories of neutrally buoyant floats in the north atlantic. *Journal of Marine Research*, *33*.

Gill, A. E. (1982). Atmosphere-ocean dynamics. *Academic press*.

LaCasce, J. H. (2008). Lagrangian statistics from oceanic and atmospheric observations. In J. B. Weiss & A. Provenzale (Eds.), *Transport and mixing in geophysical flows: Creators of modern physics* (p. 165-218). Springer Berlin Heidelberg.

Lange, M., & Van Sebille, E. (2017). Parcels v0.9: Prototyping a Lagrangian ocean analysis framework for the petascale age. *Geoscientific Model Development*, *10*(11), 4175-4186.

Large, W. G., Mcwilliams, J. C., & Doney, S. C. (1994). Oceanic vertical mixing - a review and a model with a nonlocal boundary-layer parameterization. *Reviews of Geophysics*, *32*(4), 363-403.

Liu, Y., Jing, Z., & Wu, L. (2019). Wind power on oceanic near-inertial oscillations in the global ocean estimated from surface drifters. *Geophysical Research Letters*, *46*(5), 2647–2653.

Lumpkin, R. (2016). Global characteristics of coherent vortices from surface drifter trajectories. *Journal of Geophysical Research: Oceans*, *121*(2), 1306-1321.

Lumpkin, R., & Johnson, G. C. (2013). Global ocean surface velocities from drifters: Mean, variance, El Nino-Southern Oscillation response, and seasonal cycle. *Journal of Geophysical Research: Oceans*, *118*(6), 2992-3006.

Lumpkin, R., Treguier, A.-M., & Speer, K. (2002). Lagrangian eddy scales in the northern atlantic ocean. *Journal of Physical Oceanography*, *32*(9), 2425-2440.

Lévy, M., Franks, P. J. S., & Smith, K. S. (2018). The role of submesoscale currents in structuring marine ecosystems. *Nature Communications*, *9*.

Marshall, J., Adcroft, A., Hill, C., Perelman, L., & Heisey, C. (1997). A finite-volume, incompressible navier stokes model for studies of the ocean on parallel computers. *Journal of Geophysical Research: Oceans*, *102*(C3), 5753-5766.

McGillicuddy, D. J., Anderson, L. A., Bates, N. R., Bibby, T., Buesseler, K. O., Carlson, C. A., ... Steinberg, D. K. (2007). Eddy/wind interactions stimulate extraordinary mid-ocean plankton blooms. *Science*, *316*(5827), 1021-1026.

McWilliams, J. C. (2008). The nature and consequences of oceanic eddies. In *Ocean modeling in an eddying regime* (p. 5-15). American Geophysical Union (AGU).

McWilliams, J. C. (2016). Submesoscale currents in the ocean. *Proceedings of the Royal Society A: Mathematical Physical and Engineering Sciences*, *472*(2189).

Middleton, J. F. (1985). Drifter spectra and diffusivities. *Journal of Marine Research*, *43*, 37-55.

Morrow, R., Fu, L. L., Ardhuin, F., Benkiran, M., Chapron, B., Cosme, E., ... Zaron, E. D. (2019). Global observations of fine-scale ocean surface topography with the surface water and ocean topography (SWOT) mission. *Frontiers in Marine Science*, *6*, 232.

Shakespeare, C. J., Gibson, A. H., Hogg, A. M., Bachman, S. D., Keating, S. R., & Velzeboer, N. (2021). A new open source implementation of Lagrangian filtering: A method

511 to identify internal waves in high-resolution simulations. *Journal of Advances in Mod-*
512 *eling Earth Systems*, *13*(10), e2021MS002616.
513 Taylor, J. R., & Thompson, A. F. (2023). Submesoscale dynamics in the upper ocean.
514 *Annual Review of Fluid Mechanics*, *55*, 103-127.
515 Torres, H. S., Klein, P., Menemenlis, D., Qiu, B., Su, Z., Wang, J. B., ... Fu, L. L.
516 (2018). Partitioning ocean motions into balanced motions and internal gravity waves:
517 A modeling study in anticipation of future space missions. *Journal of Geophysical*
518 *Research: Oceans*, *123*(11), 8084-8105.
519 Treguier, A. M., Deshayes, J., Le Sommer, J., Lique, C., Madec, G., Penduff, T., ...
520 Talandier, C. (2014). Meridional transport of salt in the global ocean from an eddy-
521 resolving model. *Ocean Science*, *10*(2), 243-255.
522 van Haren, H. (2003). On the polarization of oscillatory currents in the bay of biscay.
523 *Journal of Geophysical Research: Oceans*, *108*(C9).
524 Vic, C., Ferron, B., Thierry, V., Mercier, H., & Lherminier, P. (2021). Tidal and near-
525 inertial internal waves over the Reykjanes Ridge. *Journal of Physical Oceanography*,
526 *51*(2), 419–437.
527 Whalen, C. B., de Lavergne, C., Garabato, A. C. N., Klymak, J. M., MacKinnon, J. A.,
528 & Sheen, K. L. (2020). Internal wave-driven mixing: governing processes and conse-
529 quences for climate. *Nature Reviews Earth & Environment*, *1*, 606-621.
530 Yu, X., Naveira Garabato, A. C., Vic, C., Gula, J., Savage, A. C., Wang, J., ... MacK-
531 innon, J. A. (2022). Observed equatorward propagation and chimney effect of
532 near-inertial waves in the midlatitude ocean. *Geophysical Research Letters*, *49*(13),
533 e2022GL098522.
534 Yu, X., Ponte, A. L., Elipot, S., Menemenlis, D., Zaron, E. D., & Abernathey, R. (2019).
535 Surface kinetic energy distributions in the global oceans from a high-resolution nu-
536 merical model and surface drifter observations. *Geophysical Research Letters*, *46*(16),
537 9757-9766.
538 Zaron, E. D., & Elipot, S. (2021). An assessment of global ocean barotropic tide models using
539 geodetic mission altimetry and surface drifters. *Journal of Physical Oceanography*,
540 *51*(1), 63-82.

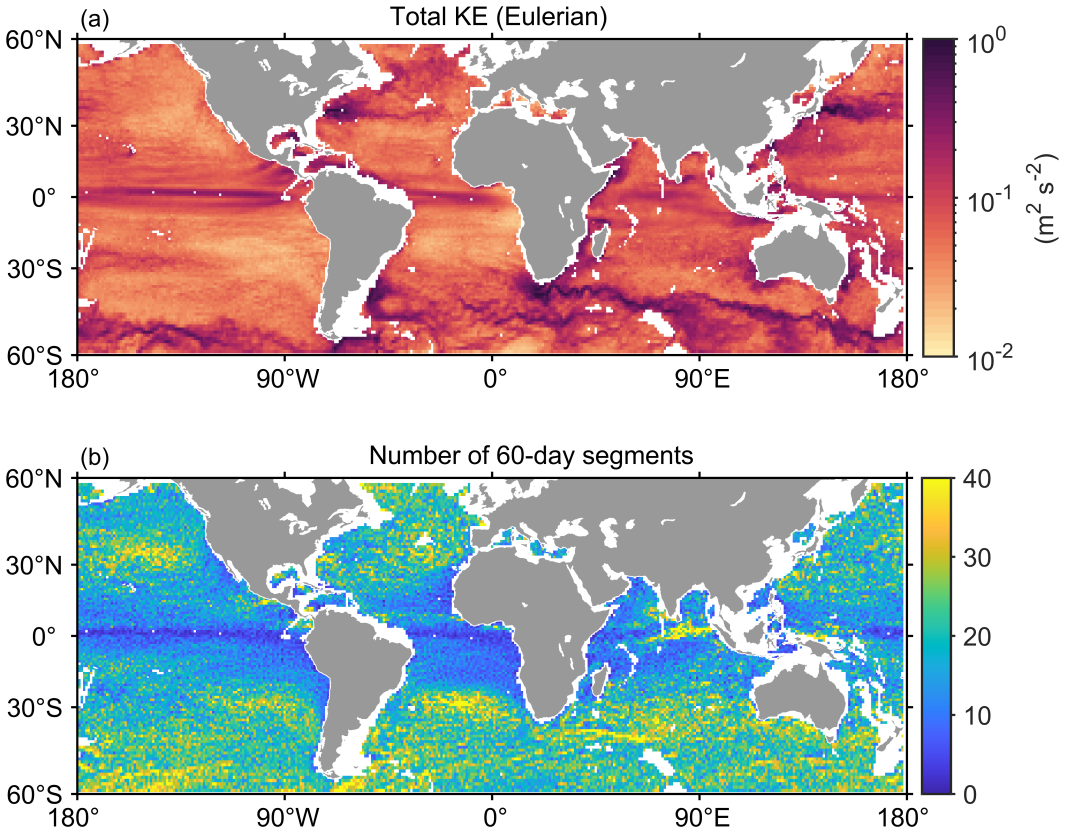

Figure 1. (a) Global map of Eulerian total KE at the surface layer in 1°× 1° bins. (b) Distribution of the number of 60-day Lagrangian trajectory segments over the global ocean in 1°× 1° bins.

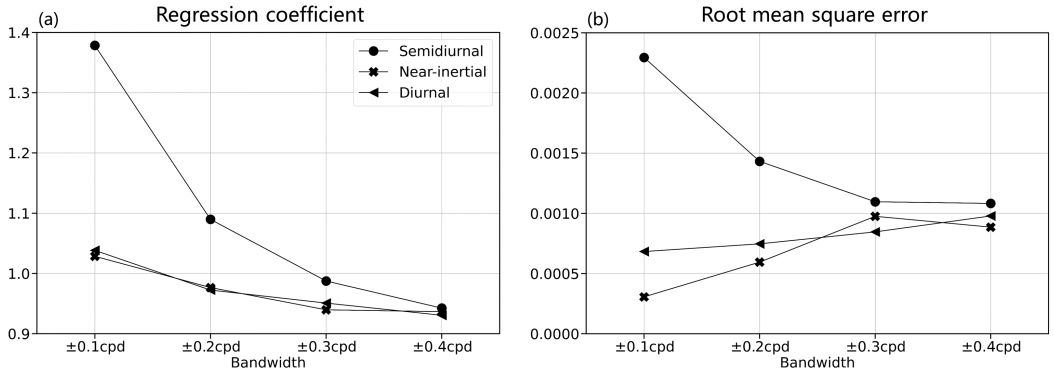

Figure 2. The (a) regression coefficient and (b) root mean square error (m^2 s^{-2}) between Lagrangian and Eulerian semidiurnal, near-inertial and diurnal KE as a function of bandwidths of ±0.1 cpd, ±0.2 cpd, ±0.3 cpd, ±0.4 cpd.

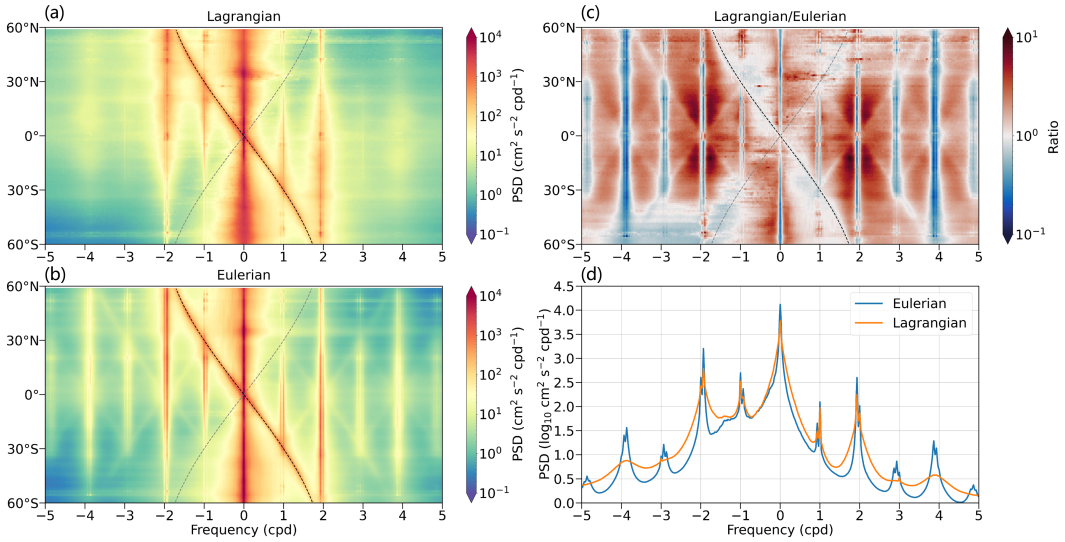

Figure 3. Zonally averaged rotary frequency spectra in 1° latitude bins from (a) Lagrangian and (b) Eulerian horizontal velocity fields at the surface layer and (c) their ratio, with positive (negative) frequencies corresponding to counterclockwise (clockwise) rotating motions, which are cyclonic (anticyclonic) in the Northern Hemisphere. The cyclonic inertial frequency ($f/2\pi$ cpd) is indicated by the gray dashed line and the anticyclonic inertial frequency ($-f/2\pi$ cpd) is indicated by the black dashed line. (d) Globally averaged anticyclonic (at negative frequencies) and cyclonic (at positive frequencies) spectra of the Eulerian (blue) and Lagrangian (orange) horizontal velocity fields.

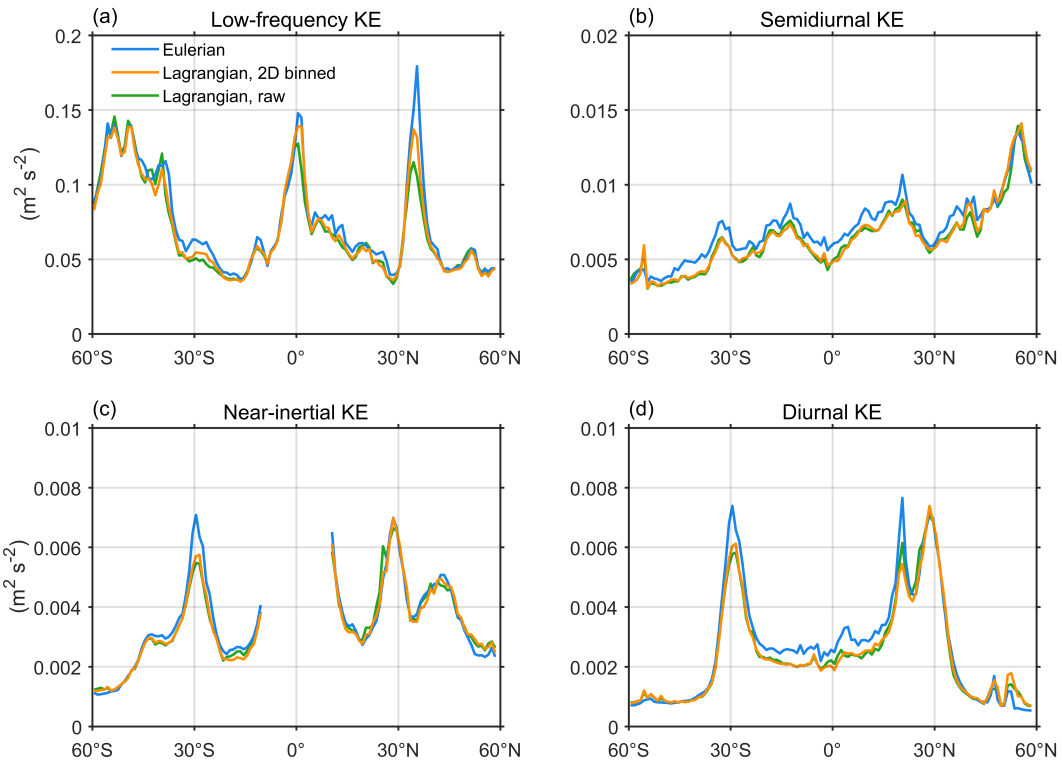

Figure 4. Zonally averaged (a) low-frequency, (b) semidiurnal, (c) near-inertial and (d) diurnal KE in 1° latitude bins estimated from Eulerian velocity field (blue) and Lagrangian particle trajectories with (orange) and without (green) binning.

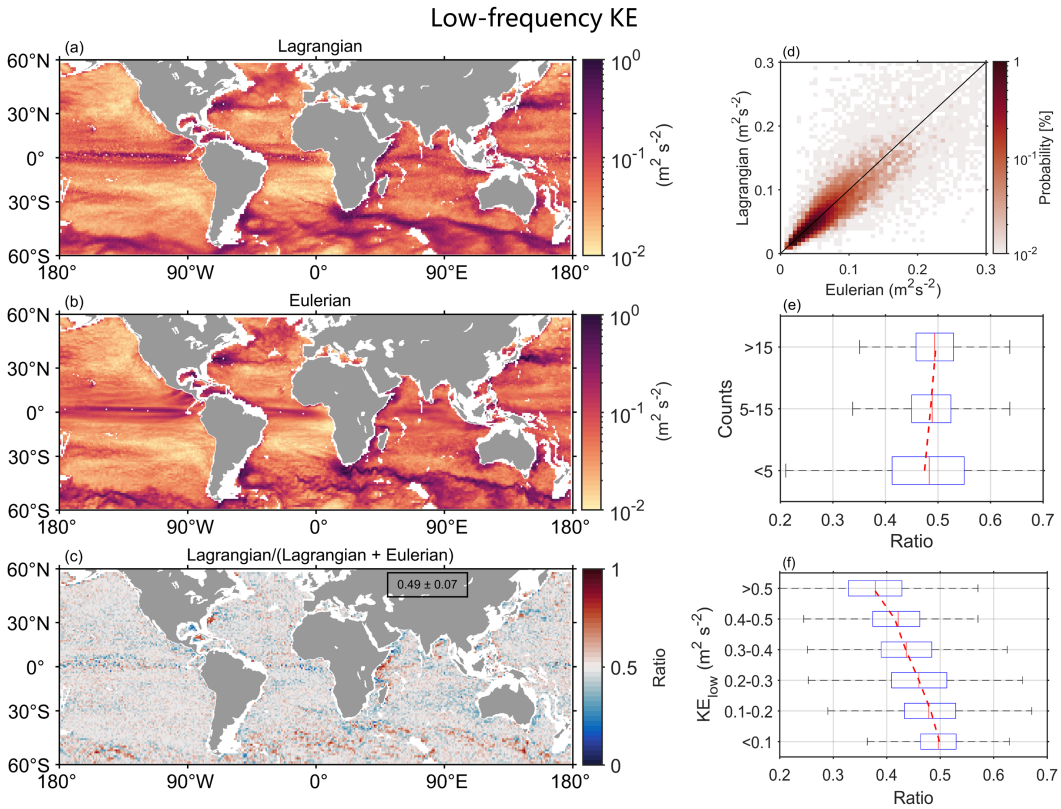

Figure 5. (a-c) Global maps of Lagrangian and Eulerian low-frequency KE at the surface layer and the ratio of Lagrangian KE/(Lagrangian KE+Eulerian KE) in 1°× 1° bins. Mean value and one standard deviation of the ratio are given in the black box in (c). (d) Joint plot of the comparison between Lagrangian and Eulerian low-frequency KE levels. (e) Box plot of the ratio under different ranges of counts of Lagrangian particles. (f) Box plot of the ratio under different ranges of low-frequency KE. The dashed red lines in (e) and (f) indicate the conditional means of the ratio.

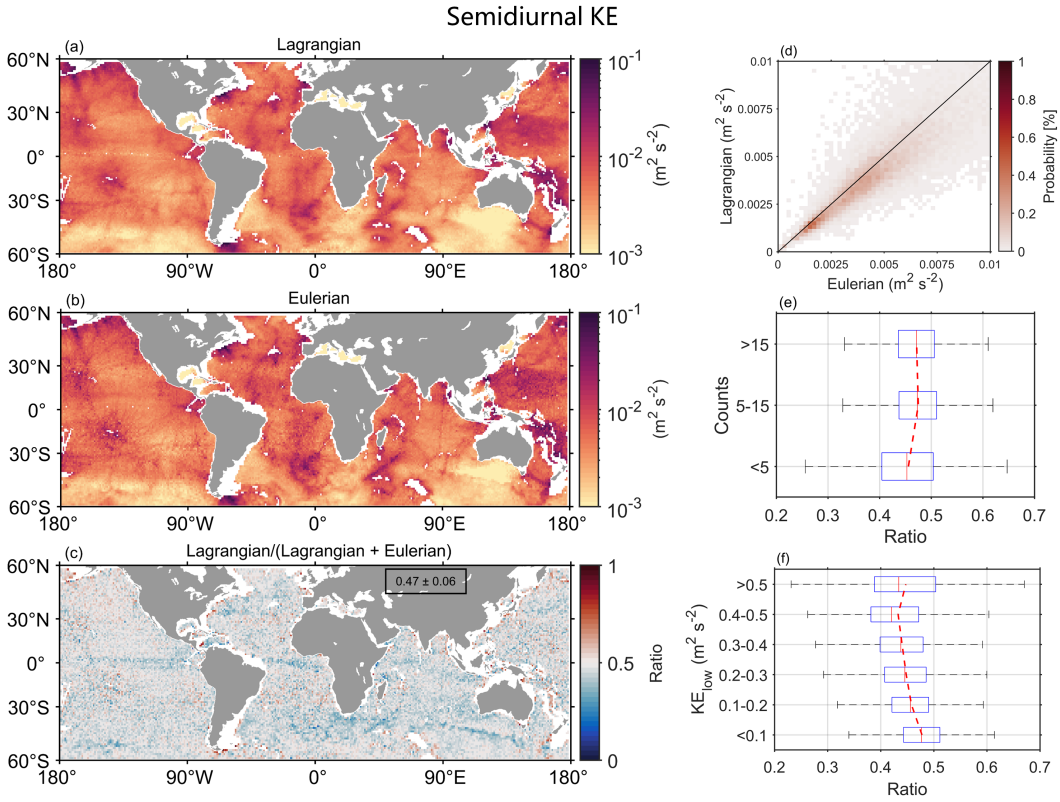

Figure 6. (a-c) Global maps of Lagrangian and Eulerian semidiurnal KE at the surface layer and the ratio of Lagrangian KE/(Lagrangian KE+Eulerian KE) in 1°× 1° bins. Mean value and one standard deviation of the ratio are given in the black box in (c). (d) Joint plot of the comparison between Lagrangian and Eulerian semidiurnal KE levels. (e) Box plot of the ratio under different ranges of counts of Lagrangian particles. (f) Box plot of the ratio under different ranges of low-frequency KE. The dashed red lines in (e) and (f) indicate the conditional means of the ratio.

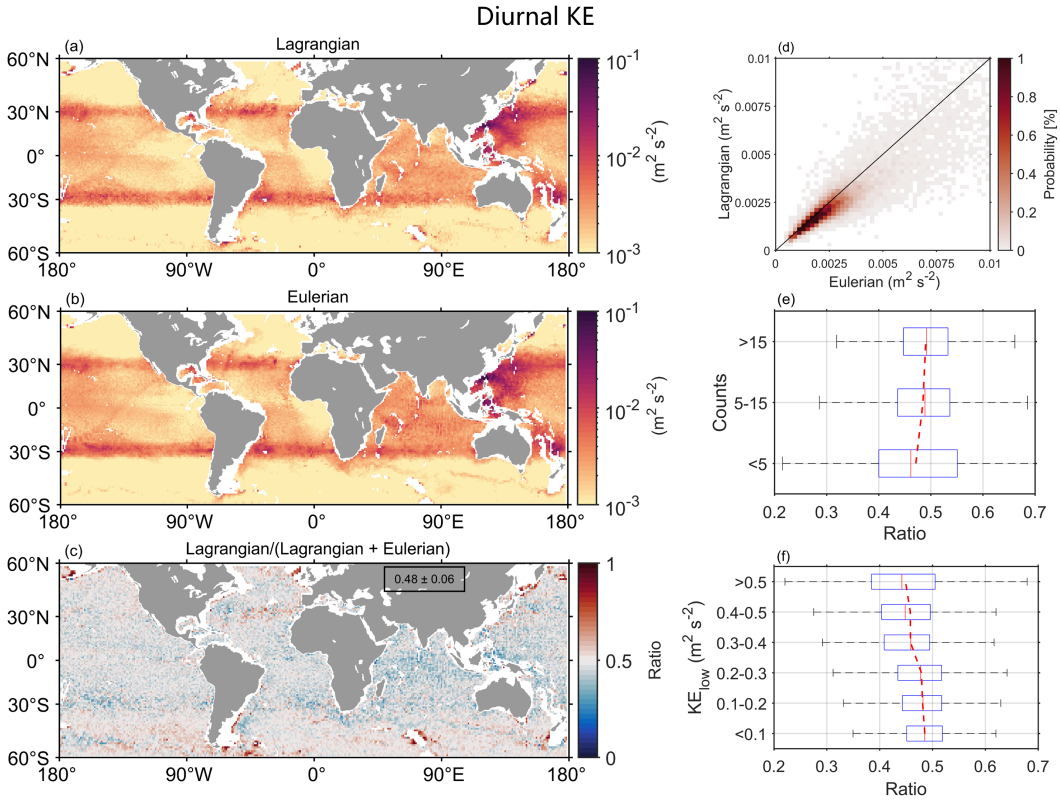

Figure 7. (a-c) Global maps of Lagrangian and Eulerian diurnal KE at the surface layer and the ratio of Lagrangian KE/(Lagrangian KE+Eulerian KE) in 1°× 1° bins. Mean value and one standard deviation of the ratio are given in the black box in (c). (d) Joint plot of the comparison between Lagrangian and Eulerian diurnal KE levels. (e) Box plot of the ratio under different ranges of counts of Lagrangian particles. (f) Box plot of the ratio under different ranges of low-frequency KE. The dashed red lines in (e) and (f) indicate the conditional means of the ratio.

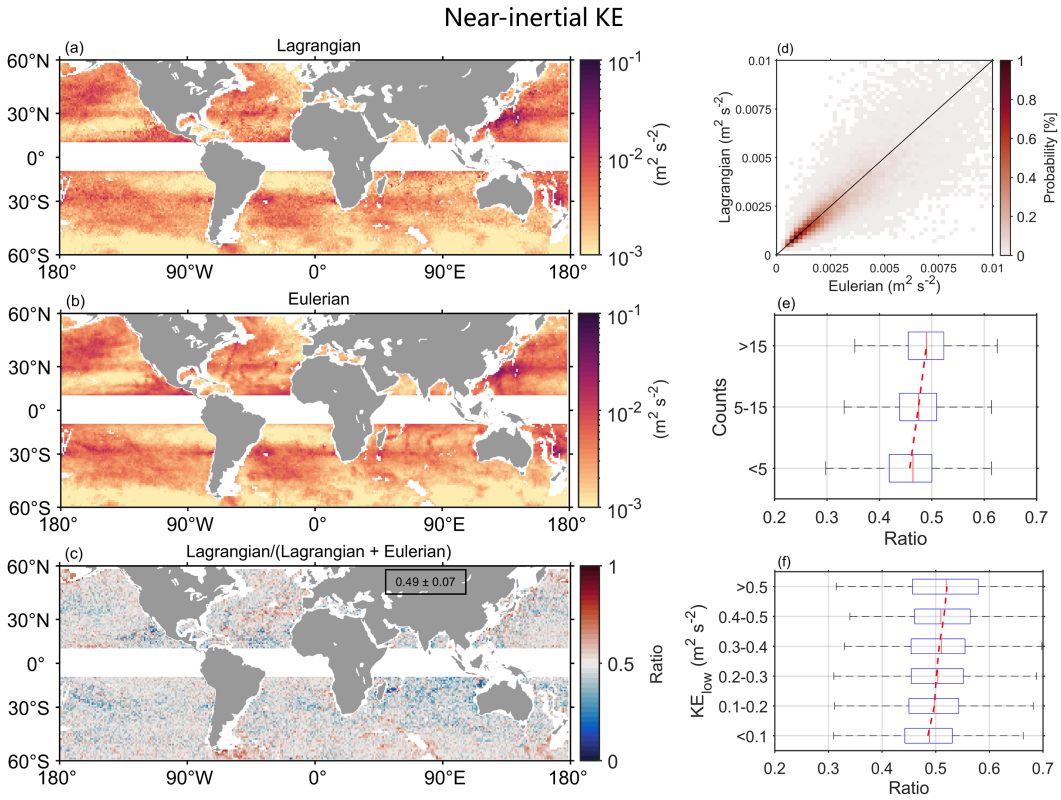

Figure 8. (a-c) Global maps of Lagrangian and Eulerian near-inertial KE at the surface layer and the ratio of Lagrangian KE/(Lagrangian KE+Eulerian KE) in 1°× 1° bins. Mean value and one standard deviation of the ratio are given in the black box in (c). (d) Joint plot of the comparison between Lagrangian and Eulerian near-inertial KE levels. (e) Box plot of the ratio under different ranges of counts of Lagrangian particles. (f) Box plot of the ratio under different ranges of low-frequency KE. The dashed red lines in (e) and (f) indicate the conditional means of the ratio.